Supplemental Material for "$MoTe_2$: A Type-II Weyl Topological Metal"

Zhijun Wang[1], Dominik Gresch[2], Alexey A. Soluyanov[2], Weiwei Xie[3], S. Kushwaha[3], Xi Dai[4], Matthias Troyer[2], Robert J. Cava[3], and B. Andrei Bernevig[1]
[1]*Department of Physics, Princeton University, Princeton, NJ 08544, USA*
[2]*Theoretical Physics and Station Q Zurich, ETH Zurich, 8093 Zurich, Switzerland*
[3]*Department of Chemistry, Princeton University, Princeton, NJ 08540, USA and*
[4]*Institute of Physics, Chinese Academy of Sciences, Beijing 100190, China*
(Dated: June 30, 2016)

Here we provide more details of the crystal structure of $MoTe_2$ at 100k, first-principles calculations, the nodal lines and Weyl points. Furthermore, the topological invariants ($\mathbb{Z}_2$ indices, Chern numbers and winding numbers) are computed for the time-reversal symmetric planes, Weyl points and nodal lines, respectively. More analysis of the surface states and Fermi arcs are presented in the last.

I. CRYSTAL STRUCTURE OF $MOTE_2$

To obtain the low temperature crystal structure of $MoTe_2$ we grew samples by slow cooling and performed diffraction measurements at 100 K to obtain the lattice constants, lattice space group, and atomic coordinates.

A. The crystal structure of orthorhombic $MoTe_2$

The crystal structure of orthorhombic $MoTe_2$, the 1T' form, was determined experimentally at 100 K by single crystal X-ray diffraction. This is a so far (with the exception of the very recent paper of Ref[1]) uncharacterized structure for $MoTe_2$, whose crystal structure has been reported previously for a hexagonal symmetry phase (the α form), 2H $MoTe_2$, and a monoclinic symmetry phase (the β form), 1T" $MoTe_2$ [2–4]. The crystal structure of the previously reported monoclinic form is related to the structure of orthorhombic WTe_2 [2], but is distorted and therefore is not isostructural with it. Thus, the orthorhombic 1T' form of $MoTe_2$ characterized here, isostructural with orthorhombic WTe_2, is the third characterized structural variant of $MoTe_2$ known; it therefore can be designated alternatively as the γ phase.

B. Experimental details

The crystals of orthorhombic $MoTe_2$ were made by slow cooling (at 1.5 K/hr) a Te-rich flux (∼95 % Te) from 1000 C to 820 C and then centrifuging off the flux. They were then annealed in a sealed evacuated quartz tube for ∼12 hours in a thermal gradient, with the crystals at 400 C and the cold end of the tube at about 60 C.

Single-crystal data were collected at 100 K on a Bruker Apex II diffractometer with Mo Kα_1 (=0.71073 Å) radiation. Data were collected over a full sphere of reciprocal space with 0.5° scans in ω with an exposure time of 30 s per frame. The SMART software was used for data acquisition. Intensities were extracted and corrected for Lorentz and polarization effects with the SAINT program. Numerical absorption corrections were accomplished with XPREP which is based on face-indexed absorption [5]. With the SHELXTL package, the crystal structure was solved using direct methods and refined by full-matrix least-squares on F^2 [6]. The largest peak in the final ΔF map was 4.91 eÅ^{-3}, 1.03 Åfrom Te1, and the largest hole was -3.94 eÅ^{-3}, located 0.98 Åfrom Mo1. The crystal refinement and atomic parameters are given in Tabs. I-II.

TABLE I. Single crystal crystallographic data for orthorhombic $MoTe_2$ at 100 K. This is the 1T' or γ form.

Refined Formula	$MoTe_2$
F.W. (g/mol)	351.14
Space group; Z	P_{mn2_1}(No.31); 4
a(Å)	3.4582(10)
b(Å)	6.3043(18)
c(Å)	13.859(4)
V(Å^3)	302.1(2)
Absorption Correction	Numerical
Extinction Coefficient	None
θ range (deg)	3.55-29.566
No. reflections	2765
No. independent reflections	899
No. parameters	38
R_1; wR_2 (all I)	0.0579; 0.1223
Goodness of fit	1.004
Diffraction peak and hole (e-/Å^3)	4.913; 3.941

C. Symmetries of the γ-phase

The crystal structure of γ-$MoTe_2$ with 4 formula units in the unit cell is shown in Fig. (1) in the main text. The corresponding point group is C_{2v} and there are three symmetry operations: the symmorphic reflection M_x, the non-symmorphic reflection M_y, and the non-symmorphic $C_{2z} = M_xM_y$ rotation. The translation accompanying the two non-symmorphic operations is $(0.5, 0, 0.5)$ in units of the lattice constants. Crucially, in the $k_z = 0$

TABLE II. Atomic coordinates and equivalent isotropic displacement parameters for orthorhombic $MoTe_2$ at 100 K. Noncentrosymmetric space group P_{mn2_1}. This is the 1T' or γ form. U_{eq} is defined as one-third of the trace of the orthogonalized U_{ij} tensor (Å^2).

Atom	Wyckoff.	Occupancy	x	y	z	U_{eq}
Mo(1)	2a	1	0	0.0297(6)	0.7384(6)	0.012(2)
Mo(2)	2a	1	0	0.6062(7)	0.2240(7)	0.014(2)
Te(1)	2a	1	0	0.2163(8)	0.1269(5)	0.015(2)
Te(2)	2a	1	0	0.6401(8)	0.8363(5)	0.012(2)
Te(3)	2a	1	0.5	0.1374(8)	0.8783(5)	0.014(2)
Te(4)	2a	1	0.5	0.7090(9)	0.0827(5)	0.010(2)

plane a little group exists at each point $(k_x, k_y, 0)$ formed by the product of time-reversal and C_{2z}, $C_{2T} = T * C_{2z}$. It is shown in Ref. [7, 8] that this symmetry allows (just like in WTe_2) for the presence of WPs in the $k_z = 0$ plane.

II. DETAILS OF NUMERICAL CALCULATIONS

The electronic structure calculations have been carried out using the all-electron WIEN2K package [9, 10]. A $15 \times 8 \times 3$ mesh and the exchange-correlation functional with a generalized gradient approximation (GGA) parametrized by Perdew, Burke, and Ernzerhof (PBE) have been used [11].

The results for the electronic band structure and topological invariants were verified versus the pseudopotential calculations done in VASP [12], using PAW [13, 14] pseudopotentials with $4s^2 4p^6 5s^1 4d^5$ and $5s^2 5p^4$ valence electron configurations for Mo and Te, respectively. Spin-orbit coupling was included in the pseudopotentials, and the PBE approximation [11] was used. Self-consistent field calculations were performed on a $16 \times 10 \times 4$ Γ-centered grid, with a Gaussian smearing of width 0.05 eV. The energy cut-off was chosen at 450 eV. Additional calculations were done using a $18 \times 15 \times 9$ Γ-centered grid, with an energy cut-off of either 260 or 300 eV, and also using a Gaussian smearing width of 0.05 eV. The experimental lattice parameters listed in Tabs. I-II are used in the calculations. To calculate the surface states, Wannier functions based tight-binding models for Mo 4d and Te 5p orbitals have been constructed [15, 16]. The topological invariants were verified with both tight-binding and *ab initio* calculations, where the Z2Pack [17] (`http://z2pack.ethz.ch/doc`) package was used for the latter.

III. BAND STRUCTURE IN THE ABSENCE OF SPIN-ORBIT COUPLING

The band structure of $MoTe_2$ exhibits several topological features in the absence of spin-orbit coupling (SOC). A clear band inversion and multiple band crossings are found in the band structure around E_F along the ΓX line, which is part of the $k_y = 0$ mirror plane. We find that the two bands $N/2$, $N/2+1$ (spin is not taken into account) cross along the ΓX line, having opposite glide-plane eigenvalues $M_y = \pm e^{-i(k_x+k_z)/2}$. Theoretical symmetry analysis [8] dictates the appearance of a line node in the $k_y = 0$ plane in case of a degeneracy on the ΓX line. Indeed, in this plane we find two nodal lines, related by M_x. The degeneracy point found on the ΓX line belongs to one of these nodal lines. In addition, 12 WPs between the $N/2$ and $N/2+1$ bands are found in $MoTe_2$ in the absence of SOC. Four of these points are located in the $k_z = 0$ plane, while the other eight appear off-plane as two quartets, symmetrically located about $k_z = 0$. One in-plane point W1 and two out of plane points W2, are listed in Tab. I of the main text, with the other 9 points related to these by M_x and M_y.

IV. WEYL POINTS BETWEEN BANDS N AND $N+1$

As described in the main text, there are 4 Weyl points (called W in the main text) formed by bands N and $N+1$ in $MoTe_2$ for the structure reported in this paper. The number N corresponds to the number of valence electrons per unit cell. These points are of type-II, as can be seen from the band dispersion obtained from first-principles calculations. The dispersion for the linearized Hamiltonian is illustrated in Fig. 1 clearly showing the Weyl point at the boundary between electron and hole pockets. A general type-II WP [7] Hamiltonian is written in terms of the Pauli matrices $\sigma_{x,y,z}$ and a kinetic term described by a unit matrix I

$$\mathcal{H}(\mathbf{k}) = \sum_{i=1}^{3} v_i k_i \; I + \sum_{i,j=1}^{3} k_i A_{i,j} \sigma_j \qquad (1)$$

where there exists a cone of directions in k-space, in which the first (kinetic) term of the Hamiltonian dominates over the second (potential) one, that is $(\sum_i v_i k_i)^2 > \sum_j (\sum_i k_i A_{i,j})^2$. Fitting the theoretical model derived from the symmetry analysis to the band structure around the WPs obtained from *ab initio* calculations results in the following effective Hamiltonian for the W WP

$$H(\mathbf{k}) = v_1 k_x + v_2 k_y + (a k_x + b k_y)\sigma_y + (c k_x + d k_y)\sigma_z + e k_z \sigma_x \qquad (2)$$

with parameters (in eVÅ) $v_1 = -3.39$, $v_2 = 0.58$, $a = 0$, $b = 0.78$, $c = 2.6$, $d = -0.58$ and $e = -0.0045$. Since there is a direction around which the kinetic energy dominates ($\hat{k} \parallel \hat{x}$), W is a type-II WP. If we limit our analysis

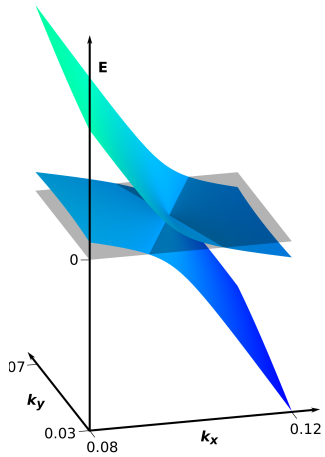

FIG. 1. Linear fit of the Weyl node W in the $k_z = 0$ plane. The plane at zero energy corresponds to the location of E_F.

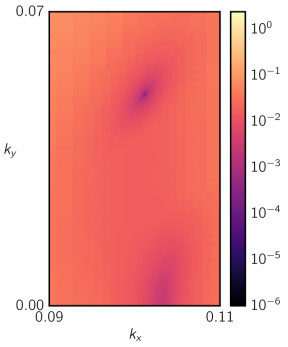

FIG. 2. The gap between bands N and $N+1$ in $MoTe_2$ at $k_z = 0$. The gap is small but non-zero on the $k_y = 0$ line, signaling a region, where additional Weyl points can arise. The point of zero gap at $k_y = 0.05$ is the Weyl point W described in the main text.

to the bands N and $N+1$ forming only 4 WPs, then $MoTe_2$ would be the simplest possible example of a TR-symmetric type-II WSM.

The previous study of Ref. [1] only considered crossings of bands N and $N+1$ and reported 8 type-II Weyl points in $MoTe_2$ in the $k_z = 0$ plane. This discrepancy arises due to the difference in the lattice parameters. Although the difference is small, the 100 K crystal structure reported here is close to the topological phase transition point, where additional Weyl points appear in pairs of opposite chirality from the $k_y = 0$ mirror plane. This can be seen in the Fig. 2, where the gap between the bands N and $N+1$ is plotted in the region of interest for $k_z = 0$ cut of the Brillouin zone. A minor change in the lattice constants can give rise to 4 additional type-II Weyl points in the $k_z = 0$ plane, as illustrated schematically in Fig. 3. Extreme sensitivity of band structure topology in $MoTe_2$ and the fact that the results of Ref. [1] are obtained for the different temperature structure suggest

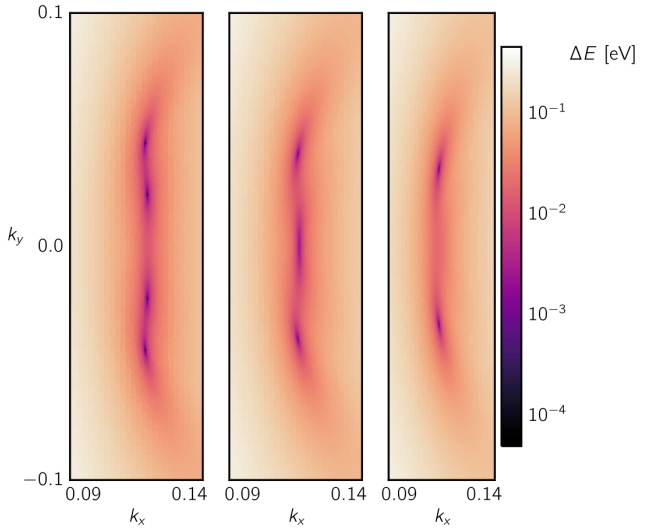

FIG. 3. Schematic illustration of the possible topological phase transition between the states of 4 and 8 type-II Weyl points which can be driven by strain.

the possibility of temperature-driven topological phase transitions in this material.

V. $\mathbb{Z}_2$ INVARIANTS AND THEIR RELATION TO WEYL POINTS

We establish a connection between $\mathbb{Z}_2$ invariants used for insulators and the existence of Weyl points. If the usual $\mathbb{Z}_2$ invariant is nonzero only on one out of the 6 common high-symmetry time-reversal symmetric (TR) planes ($k_i = 0$ and $k_i = 0.5$), the system has to exhibit Weyl points. This is easy to see. Consider the TR planes shown in the upper left panel of Fig. 4. Let only one of the planes be $\mathbb{Z}_2$ non-trivial, so that it exhibits a quantum spin Hall effect. The edge modes of the quantum spin Hall effect on this plane can result from (a) a closed surface Fermi surface such as in a weak or strong topological insulator or (b) from a disconnected open surface Fermi surface such as the Fermi arcs. Case (a), however, would imply the existence of another nontrivial $\mathbb{Z}_2$ index on one of the other TR planes (either parallel or perpendicular to the non-trivial one), hence the only possibility is that of an open Fermi arc surface state. This exercise also reveals the canonical connection pattern between Weyl points on the surface: the Fermi arcs will form the continuation of the quantum spin Hall edge states off the high-symmetry plane.

In $MoTe_2$ the valence bands and the conduction bands (N and $N+1$th bands) are directly gapped on five out of six TR planes, with the exception of the $k_z = 0$ plane that hosts four Weyl points. The appearance of Weyl points and the connection of Fermi arcs can be deduced by analyzing the $\mathbb{Z}_2$ invariants [18] for the these five TR planes. Fig. 4 shows the flow of Wannier centers [19–21] on the

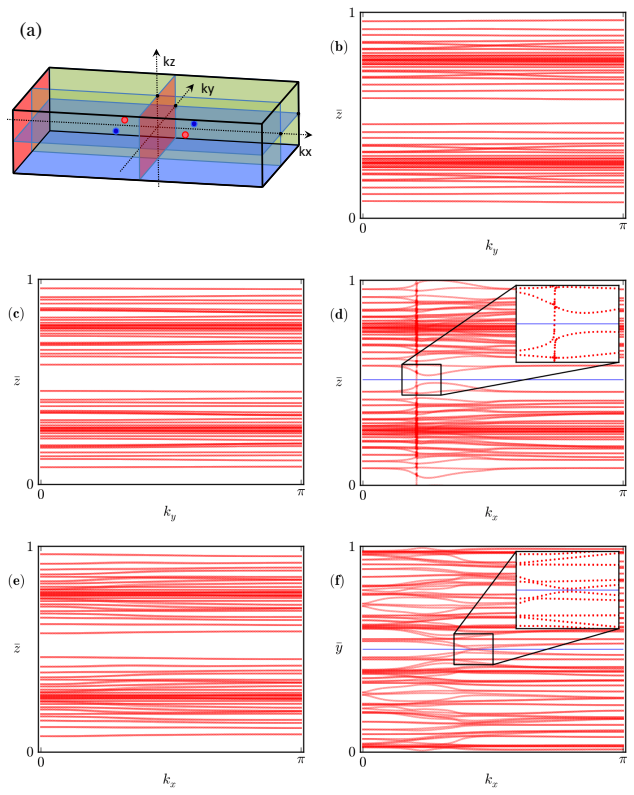

FIG. 4. Upper left panel: Six time-reversal symmetric planes are shown in the Brillouin zone. The $k_i = 0, 0.5$ planes are denoted by the red-, green-, and blue-colored sheets, for $i = x, y$ and z, respectively. Other panels show the flow of Wannier charge centers for the five gapped planes. Panel (b): $k_x = 0$; panel (c): $k_x = \pi$; panel (d): $k_y = 0$; panel (e): $k_y = \pi$; panel (f): $k_z = \pi$. The $\mathbb{Z}_2$ invariant is well defined on all except the $k_z = 0$ plane, and is non-trivial only on $k_y = 0$ plane.

five planes as calculated directly from first-principles calculations [17]. All but the $k_y = 0$ planes are $\mathbb{Z}_2$ trivial, so that the quantum spin Hall effect appears only in the xz-plane, guaranteeing that non-trivial surface states exist and cross the k_x axis on the (001) surface in accord with the surface state calculation illustrated in Fig. 6 below.

VI. TOPOLOGICAL CHARGE OF WEYL POINTS

Using the crystal symmetry C_{2v}, we only need to calculate the topological charge of the Weyl points within one-fourth of the entire Brillouin zone. The topological charge (C_S) of a Weyl point can be defined as the net flux of the Berry gauge field penetrating a 2D surface [7, 22, 23]

$$C_S = \frac{1}{2\pi} \oint_S [\nabla_{\mathbf{k}} \times \mathbf{A}(\mathbf{k})] \cdot d\mathbf{S} \qquad (3)$$

where the integrand $\mathbf{A}(\mathbf{k}) = -i\langle u_{\mathbf{k}} | \nabla_{\mathbf{k}} | u_{\mathbf{k}} \rangle$ is the Berry connection for the Bloch states $|u_{\mathbf{k}}\rangle$ calculated on the

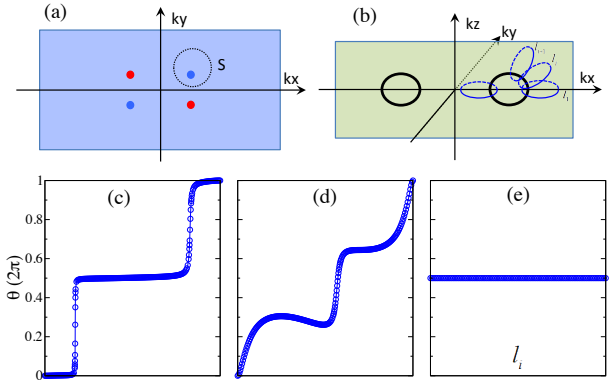

FIG. 5. (a) A sphere surrounding one of the W points is shown schematically. (b) Loops linking with the nodal line formed by bands $N-1$ and N are shown. (c) Topological charge for the point W. (d) topological charge of one of the Weyl points formed by bands $N+1$ and $N+2$, obtained by integrating the Berry curvature of $N+1$ bands. (e) The Berry phase acquired by Bloch states when going around a gapped loop linking with the nodal ring. For all loops this phase is equal to π, as expected.

surface S that encloses the Weyl node. By Stokes theorem, the C_S defined above should be equal the topological charge of the Weyl point.

For this reason, the closed Fermi surface of the type-I Weyl point has nonzero topological charge. In the case of a type-II Weyl point, however, the Fermi surface is open, and hence cannot be used to compute the topological charge of the Weyl point. Instead, we integrate the Berry curvature computed for N lowest bands, where N is the number of electrons per unit cell. A closed surface, on which the lowest N states are separated by an energy gap from the other higher energy states, and which encloses the type-II Weyl, can easily be found. This surface defines a 2D manifold in 3D momentum space, formed by the lowest N states, and unlike any possible Fermi surface, it corresponds to different energy values for different momenta $\mathbf{k}$ in the Brillouin zone.

Using both, first-principles calculations and Wannier-based tight-binding models [15, 16], Bloch states were calculated on spheres enclosing Weyl points. One of such spheres enclosing the point W of the main text is shown as a circle S in the $k_z = 0$ plane of the Brillouin zone in Fig. 5(a). For the calculation of the topological charge of Weyl points formed by bands $N+1$ and $N+2$ the Berry curvature is computed for $N+1$ bands and the integration surface is chosen such that an energy gap between $N+1$ and $N+2$ bands is present everywhere on it. For further illustration of the topological charge, following the work of Ref. [7] in Fig. 5(c-d) we plot the total electronic polarization [24] for one-dimensional circular cuts of the sphere S taken for different values of the polar angle θ for the Weyl points W and one of the points formed between bands $N+1$ and $N+2$ located at $(0.1004, 0.040, 0.0)$. The shift of polarization value when

going from $\theta = 0$ to $\theta = \pi$ gives the Chern number (chirality) of the Weyl point.

To prove the existence of the line nodes formed by bands $N-1$ and N, we calculated the Berry phase acquired by $N-1$ bands along a loop in k-space linked with one of the nodal lines, as shown if Fig. 5(b). On each of such loops a gap between bands N and $N-1$ exists, so that the Berry phase for the manifold of $N-1$ bands is a well-defined quantity. In the presence of a monopole inside the loop, this Berry phase has to be equal to π. As illustrated in Fig. 5(c), all loops have π Berry phase thus proving the existence of the line node (that is, a monopole exists within every loop).

Pierced by a line on which the bands $N-1$ and N are degenerate, while being gapped on the loop and due to the presence of the mirror plane this Berry phase is equal to π as illustrated for a set of loops in Fig. 5(e).

A. Weyls and Nodal Lines formed by bands other than N and $N+1$

We found a plethora of topological features formed by bands $N+1$ and $N+2$, including line nodes on the mirror planes and several sets of Weyl points. Of these the ones found at $\mathbf{k_1} = (0.1004, 0.040, 0.0)$, $\mathbf{k_2} = (0.11307861, 0.06131836, 0)$, $\mathbf{k_3} = (0.1603, 0.0750, 0)$, and $\mathbf{k_4} = (0.1196, 0.1068, 0.2508)$ (and their mirror images) are of the most relevant located only 60, 57, 73 and 66 meV above the Fermi level. Hidden inside the carrier pockets these additional Weyl points and their associated Fermi arcs overlap with the bulk states when projectod onto the experimentally relevant (001)-surface. The nodal lines present on the $k_x = 0$ and $k_y = 0$ planes (including the one formed by bands $N-1$ and N) also do not contribute visible spectroscopic signatures to this surface – their associated drum-head surface states [25] are projected onto the surfaces other than (001).

VII. FERMI ARCS AND SURFACE STATES

Implementing the Green's function method of Ref. [26] to the Wannier-based tight-binding Hamiltonian generalted from the first-principles calculation, we obtained the surface states for the (001)-surface. They are plotted in Fig. 6, together with the corresponding surface Fermi surfaces. As discussed above, the Weyl points formed by bands N and $N+1$ are responsible for the presence of visible surface states in the bulk gapped region. In accord with the discussion above, the surface states connecting valence and conduction states along the k_x direction are clearly seen in the spectral function of the (001)-surface of Fig. 6(a-b).

The connectivity patterns of the corresponding Fermi arcs for the (001)-surface at different energies are shown in Fig. 6(c). Since $MoTe_2$ is a type-II Weyl semimetal, the Fermi arcs are always accompanied by the projections of bulk electron and hole pockets. This makes it possible to tune the Fermi arcs by changing the position of the chemical potential, and Fig. 6(c) illustrates the evolution of the Fermi arc states for different values of the chemical potential. The states are clearly visible when this value is set to -20 meV below the Fermi level.

Unlike the case of type-I Weyl semimetals, where the Fermi arc necessarily connects the projections of the Weyl points onto the Fermi surface, here it arises out of the generic point in the electron pocket and dives back into it, as illustrated in the main text. This arc, however is still topologically non-trivial, as illustrated in Fig. 7. At small values of $|k_y| < 0.0503$ in between the two W points the 2D (k_x, k_z) cut of the Brillouin zone exhibits the quantum spin Hall effect, and the corresponding topological surface state is clearly visible connecting the valence and conduction bands across the gap (see Fig. 6(a-b)). At the position of W points, that is for $k_y = \pm 0.0503$ the corresponding 2D cut of the Brillouin zone is metallic but a surface state is still seen below the Weyl point at the boundary of the bulk valence bands projection (Fig. 7(a-b)), but it now reconnects from the valence to conduction states. At $|k_y| > 0.0503$ the 2D cuts of the Brillouin zone become topologically trivial and a topologically trivial surface state is clearly seen in Fig. 7(c-d). Thus, the Fermi arc of the main text is formed by a topological surface state, resulting from the quantum spin Hall effect at small k_y, and the topologically trivial state at larger $|k_y|$ serves to connect this in-gap state to the projections of the bulk Fermi pockets.

VIII. STRAINS

As mentioned in the main text, the band structure of $MoTe_2$ around the Fermi level is very sensitive to changes in the lattice constant. To illustrate this we studied topological phase transitions occurring between the valence and conduction bands in this material under various strain values (see Supplementary Information). We find that for these bands two additional sets of WPs can appear in $MoTe_2$ with small changes in the lattice constants. The first set consists of 4 type-II WPs in the $k_z = 0$ plane arising in pairs of opposite chirality from the mirror plane $k_y = 0$ and giving 8 total WPs in analogy with WTe_2 [7]. This scenario is realized under a hydrostatic strain of [27] $+0.3\%$ and uniaxial strains of $+2\%$ and -0.3% in z and y correspondingly. Another set of additional WPs consists of type-II nodes appearing off the $k_z = 0$ plane for a hydrostatic strain of -0.25% and for uniaxial strains of -0.2% and $+2\%$ in z and y correspondingly. Finally, both sets appear for a uniaxial strain in the x direction of 0.5% (only 0.1% strain is required to generate the additional set at $k_z = 0$), while for negative strains in x no new WPs are generated between bands N and $N+1$, but the W points move closer to each other [28]. The strong dependence of the Weyl physics on the applied strain has also been pointed out

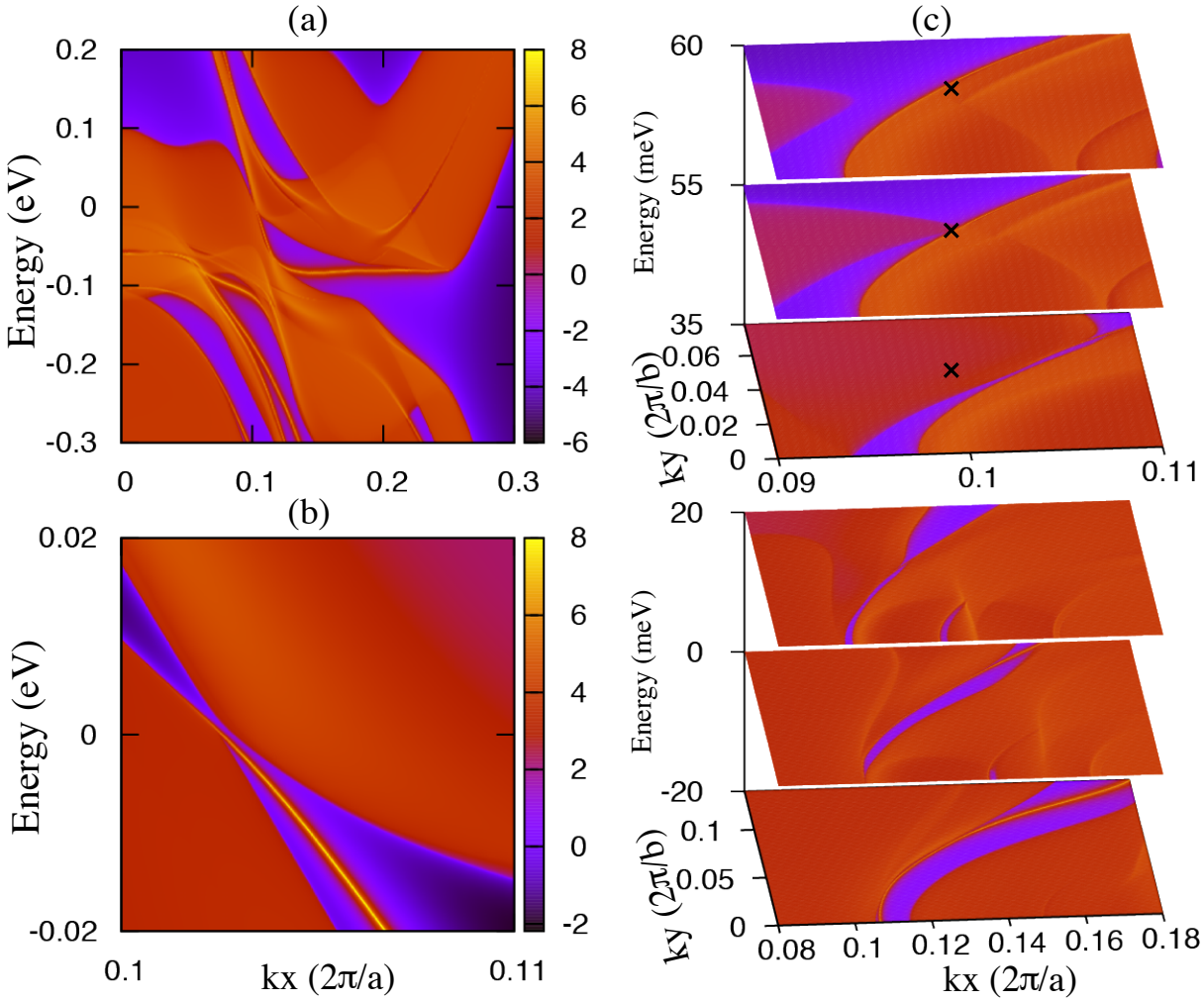

FIG. 6. Surface dispersions and Fermi surfaces. (a): (001)-surface dispersion in the k_x direction. (b): Zoom-in of panel (a), showing in-gap topological surface states. (c): The surface Fermi surfaces and Fermi arcs for different values of the chemical potential.

in [1]. For their structure, it was also found that strain can induce a type-II to type-I Weyl transition [1]. The calculation of strained structures has been performed as follows. The aim of this study was to look at the stability of different topological phases under small changes in the lattice parameters. Here the strained structures were calculated from first-principles by changing the lattice constants only, without further relaxation. To find the critical values of strains at which the topological phase transitions occur, *ab initio* calculations were performed for a large number of strained structures and the closing of the band gap at the Weyl nodes was observed. The full analysis including the calculation of topological invariants, however, was done only for specific strain values to confirm the qualitative nature of the phase transitions. The approximate values of critical strains were extracted from these calculations.

The details on the calculation of strained structures are as follows. The aim of this study was to look at the stability of different topological phases under small changes in the lattice parameters. Here the strained structures were calculated from first-principles by changing the lattice constants only, without further relaxation. To find the critical values of strains at which the topological phase transitions occur, *ab initio* calculations were performed for a large number of strained structures and the closing of the band gap at the Weyl nodes was observed. The full analysis including the calculation of topological invariants, however, was done only for specific strain values to confirm the qualitative nature of the phase transitions. The approximate values of critical strains were extracted from these calculations.

IX. ADDITIONAL REMARKS

VESTA [29], Gnuplot [30], Mayavi [31], Matplotlib [32], GIMP [33] and Inkscape [34] software pack-

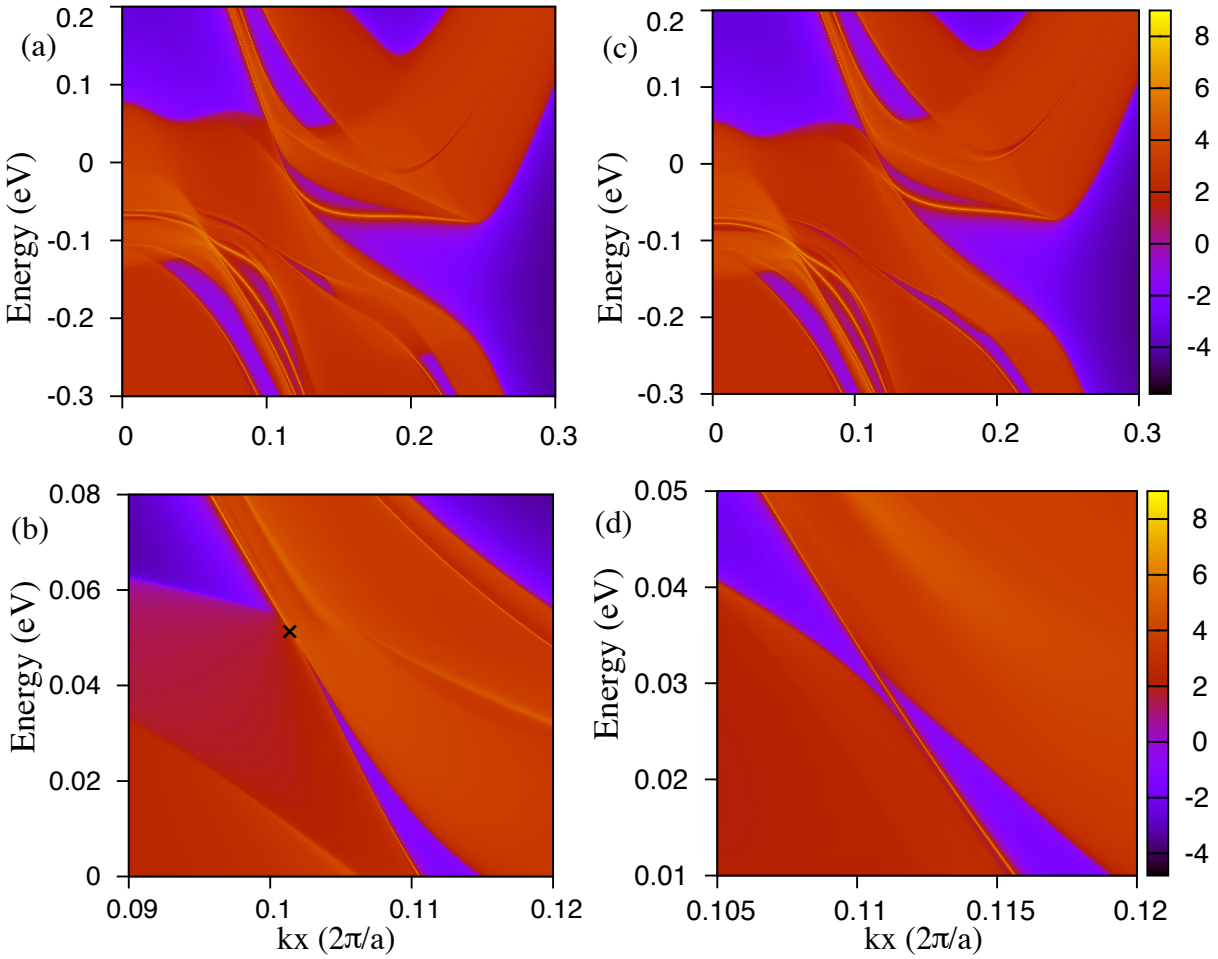

FIG. 7. Surface dispersions in the k_x direction with different k_y-values. (a): (001)-surface dispersion in the k_x direction with $k_y = 0.0503$. (b): Zoom-in of panel (a), showing a gap closure at the W Weyl point. (c): (001)-surface dispersion in the k_x direction with $k_y = 0.07$. (d): Zoom-in of panel (c), showing a trivial surface state.

ages were used to prepare some of the illustrations.

[1] Y. Sun, S.-C. Wu, M. N. Ali, C. Felser, and B. Yan, Phys. Rev. B **92**, 161107 (2015).
[2] B. E. Brown, Acta Crystallographica **20**, 268 (1966).
[3] M. Vellinga, R. De Jonge, and C. Haas, Journal of Solid State Chemistry **2**, 299 (1970).
[4] K. Ikeura, H. Sakai, M. S. Bahramy, and S. Ishiwata, APL Materials **3**, 041514 (2015).
[5] G. Sheldrick, Inc., Madison, Wisconsin, USA (2000).
[6] G. M. Sheldrick, Acta Crystallographica Section A: Foundations of Crystallography **64**, 112 (2007).
[7] A. A. Soluyanov, D. Gresch, Z. Wang, Q. Wu, M. Troyer, X. Dai, and B. A. Bernevig, Nature **527**, 495 (2015).
[8] Z. Wang, A. A. Soluyanov, J. Li, M. Troyer, and B. Bernevig, in preparation.
[9] P. Blaha, K. Schwarz, G. Madsen, D. Kvasnicka, and J. Luitz, *wien2k* (Technical Universität Wien Austria, 2001).
[10] K. Schwarz, P. Blaha, and G. Madsen, Computer Physics Communications **147**, 71 (2002).
[11] J. P. Perdew, K. Burke, and M. Ernzerhof, Phys. Rev. Lett. **77**, 3865 (1996).
[12] G. Kresse and J. Furthmüller, Computational Materials Science **6**, 15 (1996).
[13] P. E. Blöchl, Physical Review B **50**, 17953 (1994).
[14] G. Kresse and D. Joubert, Physical Review B **59**, 1758 (1999).
[15] I. Souza, N. Marzari, and D. Vanderbilt, Phys. Rev. B **65**, 035109 (2001).
[16] A. A. Mostofi, J. R. Yates, Y.-S. Lee, I. Souza, D. Vanderbilt, and N. Marzari, Computer Physics Communications **178**, 685 (2008).
[17] D. Gresch, A. A. Soluyanov, G. Autés, O. Yazyev, B. A. Bernevig, D. Vanderbilt, and M. Troyer, "Universal Framework for identifying topological materials and its numerical implementation in the Z2Pack software pack-

age," in preparation.
[18] C. L. Kane and E. J. Mele, Phys. Rev. Lett. **95**, 146802 (2005).
[19] A. A. Soluyanov and D. Vanderbilt, Phys. Rev. B **83**, 035108 (2011).
[20] A. A. Soluyanov and D. Vanderbilt, Phys. Rev. B **83**, 235401 (2011).
[21] R. Yu, X. L. Qi, A. Bernevig, Z. Fang, and X. Dai, Phys. Rev. B **84**, 075119 (2011).
[22] X. Wan, A. M. Turner, A. Vishwanath, and S. Y. Savrasov, Physical Review B **83**, 205101 (2011).
[23] Z. Wang, Y. Sun, X.-Q. Chen, C. Franchini, G. Xu, H. Weng, X. Dai, and Z. Fang, Phys. Rev. B **85**, 195320 (2012).
[24] R. D. King-Smith and D. Vanderbilt, Phys. Rev. B **47**, 1651 (1993).
[25] R. Yu, H. Weng, Z. Fang, X. Dai, and X. Hu, Phys. Rev. Lett. **115**, 036807 (2015).
[26] M. L. Sancho, J. L. Sancho, J. L. Sancho, and J. Rubio, Journal of Physics F: Metal Physics **15**, 851 (1985).
[27] Approximate values of strains are given.
[28] For a strain of -1% the W point moves to $(0.09695, 0.03356, 0)$.
[29] K. Momma and F. Izumi, Journal of Applied Crystallography **44**, 1272 (2011).
[30] T. Williams, C. Kelley, *et al.*, URL: http://www.gnuplot.info (2011).
[31] P. Ramachandran and G. Varoquaux, Computing in Science & Engineering **13**, 40 (2011).
[32] J. D. Hunter, Computing In Science & Engineering **9**, 90 (2007).
[33] G. Gimp, User manual, Edge-detect filters, Sobel, The GIMP Documentation Team (2008).
[34] M. Albert, J. Andler, T. Bah, P. Barbry-Blot, J. Barraud, B. Baxter, *et al.*, "Inkscape," (2013).